COBEM 2023 27TH INTERNATIONAL CONGRESS OF MECHANICAL ENGENEERING

ABCM Brazilian Society of Mechanical Sciences and Engineering
27th ABCM International Congress of Mechanical Engineering
December 04-08, 2023, Florianópolis-SC, Brazil

COB-2023-0030
NUMERICAL AND EXPERIMENTAL INVESTIGATION OF THE DYNAMIC BEHAVIOR OF A CONVEYOR BELT DRIVEN BY A NON-IDEAL ENERGY SOURCE

Leandro R. Oliveira
José M. Balthazar
São Paulo State University – UNESP, School of Engineering, Bauru, SP, Brazil
leandro.r.oliveira@unesp.br , jose-manoel.balthazar@unesp.br

Eduardo A. Petrocino
São Paulo State University – UNESP, School of Engineering, Bauru, SP, Brazil
eduardo.petrocino@unesp.br

Átila M. Bueno
University of Sao Paulo – USP, Polytechnic School, São Paulo, SP, Brazil
atila@lac.usp.br

Paulo J. P. Gonçalves
São Paulo State University – UNESP, School of Engineering, Bauru, SP, Brazil
paulo.paupitz@unesp.br

Marcos Silveira
São Paulo State University – UNESP, School of Engineering, Bauru, SP, Brazil
marcos.silveira@unesp.br

Maurício A. Ribeiro
Federal Technological University of Paraná, Academic Department of Mathematics – UTFPR, Ponta Grossa/PR, Brazil
Mau.ap.ribeiro@gmail.com

Ângelo M. Tusset
Federal Technological University of Paraná, Academic Department of Mathematics – UTFPR, Ponta Grossa/PR, Brazil
a.mn.tusset@gmail.com

Airton Nabarrete
Technological Institute of Aeronautics – ITA, São José dos Campos/SP, Brazil
profnabarrete@gmail.com

Abstract. *The Non-ideal systems have been largely studied in the literature and are still challenging research in the field of engineering due to their intrinsic complexity. In such systems, the dynamics of the structures influence the power source, which can be a motor. This interaction can cause the stalling motor or not achieve the specified speed for a determined power input, since, unlike ideal energy sources, the power supply is limited (called nonideal -RNIS). Different phenomena arise when there is a strong interaction between the system and the energy source, such as the resonance capture phenomena, also known in the literature as the Sommerfeld effect. In this work, the object of study is a conveyor belt system, which can be found in sugar and alcohol plants, responsible for maintaining a constant feed for the mill. For this, numerical simulations it is perform using a simplified mathematical model, which consists of a rigid body representing the conveyor belt and four springs representing the columns that support it. An unbalanced direct current motor (of limited power supply (RNIS) it is couple to the conveyor belt to perform the function of a non-ideal energy source. An experimental analysis it is also develop using IoT (internet of things) equipment, with the aim of comparing the conclusions obtained between the two methods (experimental and numerical).*
Keywords: *non-ideal machines, conveyor dynamics, Sommerfeld Effect, non-linear dynamics, Internet of Things*

1. INTRODUCTION

The motivation for the development of this research is the real application of equipment found in sugar and alcohol plants, very common in Brazil and America Latin. The sugar and alcohol production process is made up of several stages, which aim to transform sugar cane; raw material used; until its transformation into the final product, alcohol and sugar.

The first process; called receiving and preparation system; consists of removing the sugar cane from the trucks that carried out the transport, unloading it onto a feeder table, which has a characteristic inclination in order to provide the removal of mineral impurities existing in the sugar cane, since these are harmful to mechanical equipment. (HUGOT, 2014).

To carry out pre-processing of sugarcane to increase extraction efficiency in plants, equipment called a chipper breaks the sugarcane into smaller pieces using sharp knives, sending the sugarcane, now in smaller pieces, to a shredder, which will crush the sugarcane. sugarcane to open its cells, subsequently increasing the efficiency of the mills.

The flowchart of the described process is shown in figure 1.1, where the previously described equipment, feeding table, chipper and shredder are labeled in blue. Sugar cane is illustrated in green and the process flow runs from left to right. All sugarcane movement is carried out using metal conveyors, which are not the focus of this study.

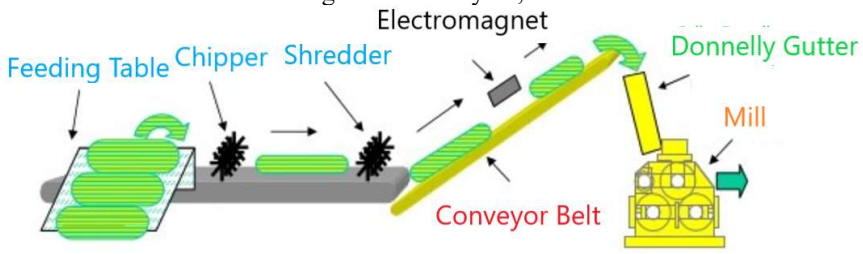

Figure 1.1 Flowchart of the Receiving, Preparation and Extraction System[Developed by the Author]

The next piece of equipment in the system is the canvas treadmill, the focus of the study of this research and in figure 1.1 it is called in red. The electromagnet, named in 1.1 in black, is located above the conveyor belt and has the objective of eliminating metallic impurities that may be present in sugarcane, since these impurities can damage the mills.

The sugar cane, now crushed; since this is the state of the sugar cane after being processed by the chipper and shredder; is taken to Chute Donelly; also known as the Donelly gutter, which works as a tank that will feed the mills and is described in 1.1 in green color. This equipment will be treated in this job as a gutter.

The purpose of the gutter is to keep the feed to the mills constant; described in 1.1 in orange color. Therefore, it is essential to keep the level at the maximum value for as long as possible, because at times when the level is not at its maximum value loss of productivity occurs. This makes the gutter level a variable that directly impacts the productivity of the system and the level is directly related to the conveyor belt, equipment that was the focus of this research study.

The gutter level also directly interferes with the efficiency of the mills, as the weight of the existing crushed sugarcane column inside the gutter will impact the amount of cane that will pass through the passage between the milling cylinders. An amount of larger material than the set will overload the milling cylinders, causing damage or shutdown of equipment due to overload.

Due to this characteristic of possibility of system shutdown due to overload, the most coherent option due to the difficulty of controlling the gutter level is to choose by keeping the level at a value below its maximum value, avoiding stops not desired.

The *DC* motor; limited energy source; is responsible for providing the movement for the conveyor belt and is attached to the structure of the canvas mat. That configuration, where the limited energy source (non-ideal source) is coupled in the structure that will be triggered is known as a non-ideal system (KONONENKO, 1969).

Non-ideal systems are not capable of influencing the source of energy limited and this energetic interaction between the source and the structure can be harmful to the equipment, mainly in the form of vibration amplitudes.

The effects presented in the form of amplitude of vibrations are due to the fact that that, at the natural frequency of the system, the structure starts to transfer energy to the source of limited energy in the form of vibrations.

This energy interaction makes the engine remain captured by resonance, as it is a limited source of energy. Once the source is capable of supplying enough energy to overcome the power the load, the *DC* motor, which was captured, jumps to a higher rotation.

The structure, in turn, while captured, presents a significant increase in vibration amplitudes and after overcoming the load power, this amplitude presents a jump to smaller values. This described behavior is known as jumping phenomenon, capture and Sommerfeld effect (KONONENKO, 1969).

Sommerfeld, in 1904, was the first to carry out an experiment analyzing systems non-ideal, using the coupling of an energy source (*DC* motor) to a flexible structure. In this experiment, contrary to expectations, the *DC* motor showed fluctuating values of angular velocity despite continuing to increase the voltage same armor. This phenomenon observed by Sommerfeld was studied by Kononenko (KONONENKO, 1969). Other authors have also addressed this problem as Nayfeh and Mook (NAYFEH; MOOK, 2008), and Balthazar (BALTHAZAR et al., 2001; BALTHA ZAR et al., 2003a; BALTHAZAR et al., 2018; BALTHAZAR et al., 2003b; BALTHAZAR, 2022) and several other authors who, although not highlighted in this research, contributed to the development of the study of this phenomenon.

Due to these studies, several problems related to non-ideal systems have been studied and observed in recent scientific publications, where many analyzes non-linear methods consider the excitation of structures or mechanical systems as a

function of the vibration displacement, speed, etc. Considering real problems, the system vibration affects the energy source, mainly close to resonance behavior.

1.1 Materials and Methods

The development of the numerical simulations are carried out through the Matlab® software using the numerical method of fourth-fifth order of Runge-Kutta, having as parameters for the relative error tolerance and absolute error tolerance the standard function values that correspond, respectively, 0.001 and 0.000001, once that these parameters define the acceptable error for each step in solving the equations differentials of the motion of the system, which were developed through the equations of Lagrange.

The natural frequencies of the model were also identified, considering that it is in the natural frequencies that the manifestation of the Sommerfeld effect occurs, analyzing also the impact that the vibrations of the system will generate in the structure of the treadmill.

The experimental analysis is performed using an Arduino microcontroller shown in figure 1.2 (a). Because it is a code prototyping platform free, Arduino allows the development of applications that require a controller through programming in C language. Due to its characteristic of having inputs and outputs, it is possible to drive DC motors, as well as reading variables through sensing in the most diverse ways.

The optical encoder type sensor, model LM 393, shown in figure 1.2 (b) performs speed measurement through calculations that correlate interruption detection of light with the angular speed of the DC motor.

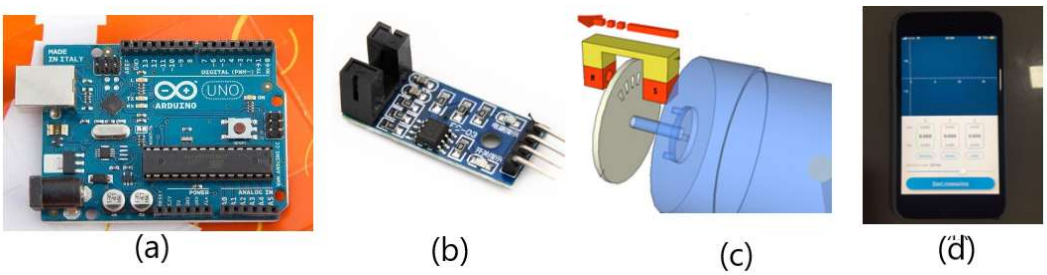

Figure 1.2 Arduino (a) and optical encoder type sensor, model LM 393 (b) [Image available at https://www.embarcados.com.br/arduino-uno. Accessed on 04-28-2021.] (c) Speed Measurement Strategy Used Speed Measurement Angular [Image available at https://www.arduinoecia.com.br/sensor-de-velocidade-lm393-arduino/. Accessed on 2022-06-20.] (d) Iphone 6 Used to Measure Vibrations[Developed by the author]

Figure 1.2 (c) illustrates the similar strategy used to measure angular velocity, where coupled to the motor shaft is a disc with 4 holes that will allow the passage of the beam of light coming from the emitter. The receiver will pick up the beam of light, sending an electrical signal to the digital input of the Arduino. a number of interruptions equal to the number of holes in the disc corresponds to one rotation, allowing in this way, measure the angular velocity of the *DC* motor.

To carry out the experimental analysis, a 3D printer model Ender-3 V2 from manufacturer Creality is used to develop the apparatus that will represent the treadmill shipping company. It is composed of a structure formed by a rigid body supported by 4 aluminum springs with a diameter of 5 cm, similar to the spirals used to join the pages of notebooks. The springs have pairs of different sizes in order to obtain the inclination found in the real equipment used as motivation for this research. This inclination can be understood through the representation of the conveyor belt in figure 1.1.

The measurement of vibrations is carried out using an iPhone 6 model cell phone that can be seen in figure 1.4. It has an accelerometer that allows to identify vibrations through various applications available for free.

2. MATHEMATICAL MODELING

The system model consists of a rigid body supported by four springs as previously described. The unbalanced DC motor is fixed to the rigid body; which represents the conveyor belt; and acts as a limited non-ideal energy source. The four springs, with stiffness constants defined as k1e, k1d, k2e and k2d and damping coefficients defined as c_{1e}, c_{1d}, c_{2e} and c_{2d} have size pairs equal, where k_{1e}, k_{1d} have the same size and k_{2e} and k_{2d} also have the same size. In this way, the inclination found in the real equipment is obtained. All stiffness and damping coefficients have the same value, but we chose differentiates them in order to provide information about their location in the model.

This model was inspired by the work of (ALIŞVERIŞÇI et al., 2015), who performed a similar experiment, but designed for only 3 degrees of freedom; with the perspective of the plan; demonstrating the presence of non-linear vibrations in its work. For this research it was one more degree of freedom was inserted, and the model was analyzed in three dimensions.

Figure 2.1 demonstrates the model and geometric relationships, where the rigid body represents the conveyor belt and the lengths have been defined using the center of mass of the structure as a reference. These lengths, called *a*, *b*, *c* and *d* represent the size of the conveyor belt, *h* represents the length between the vector of action of the of vertical force and the center of mass of the structure *C*, and represents the length between the center of mass *C* and the center of the shaft of the DC motor *B*. The variable *r* represents the length between and the center of the shaft of the *DC* motor *B* and the position of the unbalanced mass *A*, where the mass m_2 is fixed.

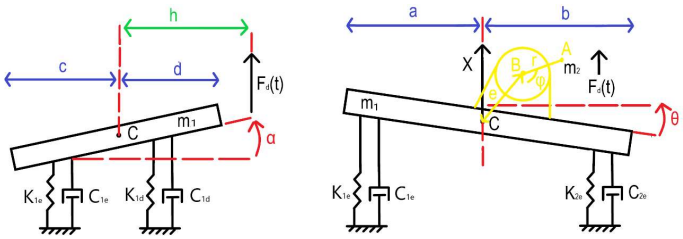

Figure 2.1 Model Representation [Developed by the author]

The system was modeled to obtain the transverse angular variations, through the angle α, and the longitudinal angular variations, through the angle θ. the displacement vertical is represented by *x*. The mass of the conveyor belt is represented by m_1 and the unbalanced mass of the *DC* motor per m_2. Figure 3.1 demonstrates the relationships model geometry.

A conveyor belt is shown in figure 3.2(a). Figure 3.2 and (b) and (c), demonstrate the model used in this work that was used for 3D printing and subsequently used for experimental simulations.

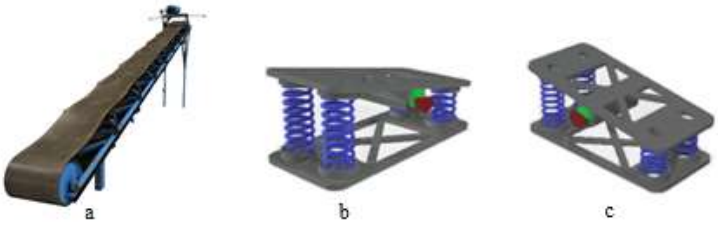

Figure 2.2 3D Model of a Real Treadmill (a) and Model of the Used System for That Work (b, c). (a: [Image Available at https://www.turbosquid.com/3D-Models/3d conveyor-belt-model/827002?referral=3dsecure. Accessed on 04-28-2021.]; b, c: Elaborated by the Author]

2.1 Governing Equations of Motion

The generalized coordinates illustrated in figure 2.1 representing the geometric relationships were selected as *x*, which represents the vertical displacement of the belt, θ, which represents the longitudinal angular displacement, and α, which represents the displacement transverse angle.

The *DC* motor was coupled in the equations as the responsible non-ideal energy source for producing the excitation of the system. It was modeled using the equations of Lagrange, where its generalized coordinate is Φ, which represents the angular velocity of the *DC* motor axis, making it possible to analyze the longitudinal angular displacements and transverse and, the vertical linear displacement of the conveyor belt, using the Lagrangian equations in the form:

$$\frac{d}{dt}\left(\frac{\partial L}{\partial \dot{q}_k}\right) - \frac{\partial L}{\partial q_k} + \frac{\partial R}{\partial \dot{q}_k} = Q_k;\ L = T - U \tag{1}$$

Where, *L* is the Lagrangian, *T* is the kinetic energy, *U* is the potential energy, *R* Rayleigh Dissipation Function, q_k are the generalized coordinates and Q_k are the generalized forces.

The energy equations obtained for the system are represented by Eq. 2 and Eq. 3

$$T = \frac{1}{2}(m_1 + m_2)\dot{x}^2 + \frac{1}{2}J_L\dot{\theta}^2 + \frac{1}{2}J_B\dot{\alpha}^2 + \frac{1}{2}J_0\dot{\varphi}^2 + \frac{1}{2}m_2e^2\dot{\theta}^2 + \frac{1}{2}m_2r^2\dot{\varphi}^2 + m_2re\dot{\theta}\dot{\varphi}\sin\varphi + m_2(-e\dot{\theta}\sin\theta + r\dot{\varphi}\cos\varphi)\dot{x} \tag{2}$$

$$U = \frac{1}{2}k_{1e}y^2_{1e} + \frac{1}{2}k_{1d}y^2_{1d} + \frac{1}{2}k_{2e}y^2_{2e} + \frac{1}{2}k_{2d}y^2_{2d} + m_2gr\sin(\varphi + \theta) \tag{3}$$

Selecting as generalized coordinates the variables $q1 = x$, $q2 = \theta$, $q3 = \alpha$ and $q4 = \Phi$, the equations of motion for generalized coordinates are given by equations 4, 5, 6 and 7.

$$(m_1 + m_2)\ddot{x} + (c_{1e} + c_{1d} + c_{2e} + c_{2d})\dot{x} + [-(c_{1e} + c_{1d})a + (c_{2e} + c_{2d})b]\dot{\theta} + [-(c_{1e} + c_{2e})c + (c_{1d} + c_{2d})d]\dot{\alpha} + (k_{1e} + k_{1d} + k_{2e} + k_{2d})x + [-(k_{1e} + k_{1d})a + (k_{2e} + k_{2d})b]\theta + [-(k_{1e} + k_{2e})c + (k_{1d} + k_{2d})d]\alpha = -m_2(-e\dot{\theta}\sin\theta - e\theta^2\cos\theta + r\ddot{\varphi}\cos\varphi - r\dot{\varphi}^2\sin\varphi) \quad (4)$$

$$(J_L + m_2e^2)\ddot{\theta} + \left[(c_{1e} + c_{1d})a^2 + (c_{2e} + c_{2d})b^2\right]\dot{\theta} + [(c_{1e}c - c_{1d}d)a - (c_{2e}c - c_{2d}d)b]\dot{\alpha} + [(c_{1e} + c_{1d})a - (c_{2e} + c_{2d})b]\dot{x} + [(k_{1e} + k_{1d})a^2 + (k_{2e} + k_{2d})b^2]\theta + [(k_{1e}c - k_{1d}d)a - (k_{2e}c - k_{2d}d)b]\alpha + [(k_{1e} + k_{1d})a - (k_{2e} + k_{2d})b]x = -m_2re\ddot{\varphi}\sin\varphi + m_2re\dot{\varphi}^2\cos\varphi - m_2e\ddot{x}\sin\theta \quad (5)$$

$$(J_B + m_2r^2)\ddot{\alpha} + [(c_{1e} + c_{2e})c^2 + (c_{1d} + c_{2d})d]\dot{\alpha} - [(c_{1e} - c_{1d})c - (c_{1d} + c_{2d})d]\dot{x} + [(c_{1e}c + c_{1d}d)a - (c_{2ec} + c_{2dd})b]\dot{\theta} + [(k_{1e} + k_{2e})c^2 + (k_{1d} + k_{2d})d^2]\alpha - [(k_{1e} - k_{2e})c - (k_{1d} + k_{2d})d]x + [(k_{1e}c + k_{1d}d)a - (k_{2e}c + k_{2d}d)b]\theta = -m_2(-e\dot{\theta}\sin\theta - e\theta^2\cos\theta + r\ddot{\varphi}\cos\varphi - r\dot{\varphi}^2\sin\varphi).h \quad (6)$$

$$(J_0 + m_2r^2)\ddot{\varphi} + m_2re\dot{\varphi}\sin\varphi + m_2rcos\varphi\ddot{x} + m_2gr\cos\varphi = \tau(\Phi) \quad (7)$$

Where τ represents the torque available on the DC motor shaft as a function of speed according to Eq. 8.

$$\tau(\dot{\Phi}) = M_0\left(1 - \frac{\dot{\Phi}}{\Omega_0}\right) \quad (8)$$

The variable g represents the gravitational constant used to calculate the force gravity exerted on the structure. J_L and J_B are, respectively, the moments of inertia of the conveyor belt for the longitudinal angular displacements and cross section, J_0 is the inertia constant of the *DC* motor and r is the distance between the centers of the *DC* motor shaft and the position of the unbalanced mass m_2 connected to the motor shaft *DC*. The variables that represent the lengths of the structure can be found in figure 2.1.

To obtain the behavior of the power limited DC motor and represent the torque as a function of angular velocity, two parameters M_0 and Ω_0 are used, which respectively, is the torque constant of the *DC* motor and the maximum torque frequency.

According to figure 2.3 (a), when the angular velocity Φ is equal to zero, the torque M_0 is maximum, that is, the torque value transmitted to the *DC* motor shaft and, consequently, transformed into force to move the conveyor belt.

As the angular velocity increases, the torque available at the motor shaft *DC* decreases linearly as shown in figure 2.3 (b), reaching a value equal to zero, and Ω_0 represents the angular velocity when the torque available on the motor shaft CC is zero.

However, the actual curve of torque versus speed of a *DC* motor is not linear, as shown in Fig. 2.3(b), but non-linear, as illustrated 2.3(c).

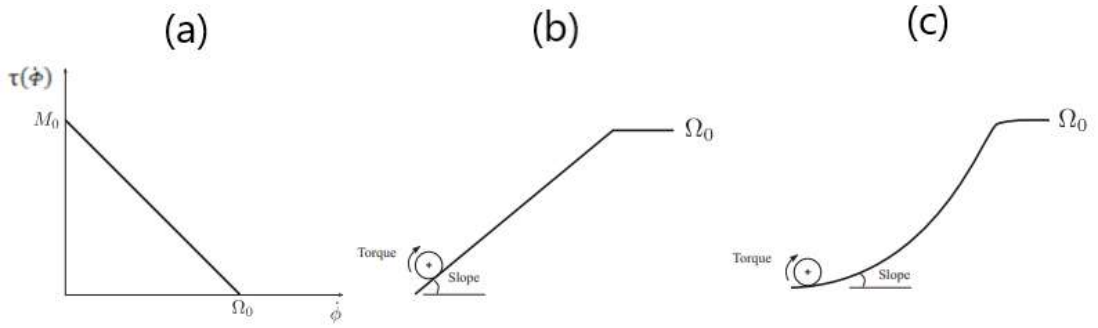

Figure 2.3 Torque Characteristic Curve (a) for linear (b) and non-linear (c) motor *DC* (GONÇALVES et al., 2014a).

To obtain the engine acceleration effect between the initial and final torque, it is necessary to define Ω_0 as a time-dependent function according to Eq. 3.9. Of that in this way, it is possible to simulate the acceleration of the motor in the same parameters used in the experimental analysis.

$$\Omega_0\,(t) \;=\; \frac{\Omega_2 \;-\; \Omega_1}{t_2}\;\; t \tag{9}$$

Thus, the torque value becomes dependent on Ω_2 which is the angular velocity when the torque is zero, and Ω_1 the initial angular velocity when the torque is maximum.

The variable t_2 represents the acceleration time for the variation of the *DC* motor between initial angular velocity Ω_1 and final angular velocity Ω_2.

The t_2 variable directly influences the way in which the effect is manifested Sommerfeld, where a faster pass through the resonant frequency causes the capture of the angular speed of the *DC* motor presents speed fluctuations of different ways.

3. NATURAL FREQUENCYS ANALYSIS

The characteristic equation for an invariant linear system in the time is developed, thus finding the vibration modes of the structure, performing a comparison of the influence of the linear displacement of the structure on the displacements angles selected for visualization of vibration models.

Using the equations of motion found in Eq 4, 5, 6 and 7, the same equations can be rearranged and rewritten in matrix form as:

$$\begin{bmatrix} m_{11} & 0 & 0 \\ 0 & m_{22} & 0 \\ 0 & 0 & m_{33} \end{bmatrix}\begin{bmatrix} \ddot{x} \\ \ddot{\theta} \\ \ddot{\alpha} \end{bmatrix} + \begin{bmatrix} k_{11} & k_{12} & k_{13} \\ k_{21} & k_{22} & k_{23} \\ k_{31} & k_{32} & k_{33} \end{bmatrix}\begin{bmatrix} x \\ \theta \\ \alpha \end{bmatrix} = \begin{bmatrix} F \\ Fg \\ Fh \end{bmatrix} \tag{9}$$

The characteristic equation for a time-invariant linear system f is given by:

$$f \;=\; det\,[K_m \;-\; \lambda M_m] \tag{10}$$

That $\lambda = \omega^2$. To solve the Eq. 10 and find the natural frequencies, the values in the table 3.1 were used.

Table 3.1. Parameters used for numerical simulations

Parameters	Values
Stiffness Coefficients k_{1e}, k_{2e}, k_{1d},k_{2d}	**193 N/m**
Damping Coefficients c_{1e},c_{2e},c_{1d}, c_{2d}	**0.01 N s/m**
Distance a	**0.08 m**
Distance b	**0.05 m**
Distance c	**0.05 m**
Distance d	**0.04 m**
Radius r	**0.015 m**
Distance e	**0.015 m**
Distance h	**0.15 m**
DC Motor Inertia Constant J_0	**1e-4 N m2**
DC Motor Torque Constant M_0	**5e-2 N m**
Mass of Conveyor Belt m_1	**0.23 Kg**
Unbalance Mass m_2	**4.8e10-3 Kg**
Moment of Inérica J_L	**15e10-6 N m2**
Moment of Inérica J_B	**9e10-6 N m2**

The resulting natural frequencies are ω_1 = 59.01 *rad/s*; ω_2 = 119.77 *rad/s* and ω_3 = 176.92 *rad/s*. It is possible to notice that the relations between the obtained natural frequencies are approximately 1:1 and 1:2, the same ratios obtained in the works of (TSUCHIDA et al., 2003; TSUCHIDA; WILLIAM; BALTHAZAR, 2005; FELIX et al., 2002).

For free vibration, we consider a harmonic solution:

$$X\,cos\,(\omega t \;+\; \varphi), \theta\,(t) \;=\; \Theta\,cos\,(\omega t \;+\; \varphi), \alpha\,(t) \;=\; A\,cos(\omega t \;+\; \varphi) \tag{11}$$

Using Eq. 11 obtained Eq. 12:

$$\begin{bmatrix} -m_{11}\omega^2 \;+\; k_{11} & k_{12} & k_{13} \\ k_{21} & -m_{22}\omega^2 \;+\; k_{22} & k_{21} \\ k_{31} & k_{32} & -m_{33}\omega^2 \;+\; k_{33} \end{bmatrix}\begin{bmatrix} X \\ \Theta \\ A \end{bmatrix} = \begin{bmatrix} 0 \\ 0 \\ 0 \end{bmatrix} \tag{12}$$

With the values obtained previously, we can determine the ratio between the amplitudes by Eq. 12:

$$\frac{X^{(n)}}{\Theta^{(n)}} = u_1{}^{(n)} \tag{13}$$

$$\frac{X^{(n)}}{A^{(n)}} = u_1{}^{(n)} \tag{13}$$

Where u_1 is the distance between the node and the center of mass for longitudinal displacement and u_2 is the distance between the node and the center of mass for transverse displacement. The values for each vibration mode are shown in Table 3.2. It demonstrates the values obtained, where for the third mode of vibration, for each unit of displacement in x, a large angular displacement by α is performed. It is concluded that the third mode of vibration represents a limit that must be avoided, jeopardizing the integrity of the equipment.

Table 3.2. Distance between nodes u1 and u2 and the Model Center of Mass

Vibrate Modes	Values
Mode 1	$u_1{}^{(1)}$
	$u_2{}^{(1)}$
Mode 2	$u_1{}^{(2)}$
	$u_2{}^{(2)}$
Mode 3	$u_1{}^{(3)}$
	$u_2{}^{(3)}$

In figure 4.1 the projection of the distances obtained in table 4.2 is shown and the lines dashed lines illustrate the angular displacements of α and θ, allowing you to visualize how the offsets from each angle will occur according to the front and horizontal views of the equipment.

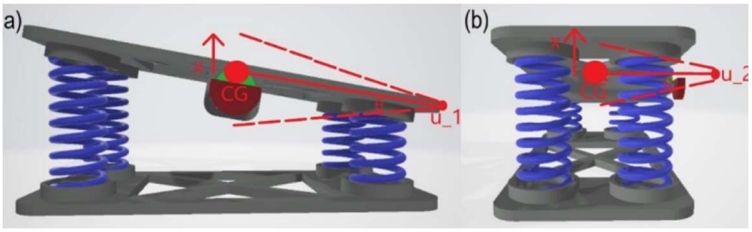

Figure 3.1 Conveyor Belt Vibration Modes [Developed by the author]

Normalization was performed to determine the angular variations for each variation unit x, making it possible to determine the influence of each vibration mode in transverse and longitudinal angular movements.

4. NUMERICAL RESULTS

The numerical simulation was performed using as initial conditions: $y_1 = 0$; $y_2 = 0$; $y_3 = 0$; $y_4 = 0$; $y_5 = 0$; $y_6 = 0$; $y_7 = 0$, $y_8 = 0$ and the same parameters as in table 3.1.

Matlab® software was used to numerically solve the differential equations through the fourth and fifth order Runge-Kutta method.

For the simulation, the values of $\Omega_1 = 1$, $\Omega_2 = 857$ and $t_2 = 300$ were used as non-ideal parameters of the DC motor, chosen in order to represent the same parameters of the engine used in the experimental analysis.

Figure 4.1 (a) represents the angular velocity of the *DC* motor with its evolution demonstrated in time. The figure demonstrates two regions where the motor presents fluctuations in its angular velocity, due to the entry into the resonance region of the structure. The frequency jump is also clearly visualized, demonstrated by a vertical line in the frequency values.

Figure 4.1 (b) represents the linear displacement of the structure, where the increase in the vibration amplitudes of the structure with a subsequent decrease in approximately 50 ***s***, the same region where the fluctuation in velocity is observed angle of the motor in figure 4.1 (a). The increase in vibration amplitudes occurs until approximately 90 *s*, when the amplitude decreases. Again, a notable increase, this time more modest, in the vibration amplitudes until approximately 160 *s* when, again, the characteristic decrease of the Sommerfeld effect occurs. After 160 *s*, an increase in vibrations is visualized, but with oscillatory values between high and low amplitudes.

Figure 4.3 (c) represents the transversal angle of the structure, where the increase in the vibration amplitudes of the structure with subsequent sudden decrease in approximately 50 *s* just like figure 4.1 (b). For this figure, it is observed still regions where the increase in vibration amplitudes occurred in a significant way, as in approximately 160 *s*, but the decrease does not occur in a significant way abrupt as is characteristic of the Sommerfeld effect, being gradually reduced until approximately 220 *s*. After that, the same oscillations between highs and lows are observed amplitude values of figure 3.1(b).

Figure 4.1 (d) represents the structure's longitudinal angular displacement, demonstrating the increase in the structure's vibration amplitudes that starts in approximately 90 s. The increment in the vibration amplitude values occurs from characteristic manner of the Sommerfeld effect, with the sharp reduction occurring in approximately 160 *s*. After this moment, there is an increase in the amplitudes with subsequent stagnation of values, not showing the same characteristics of high and low oscillatory values shown by figures 3.1 (b) and 3.1(c).

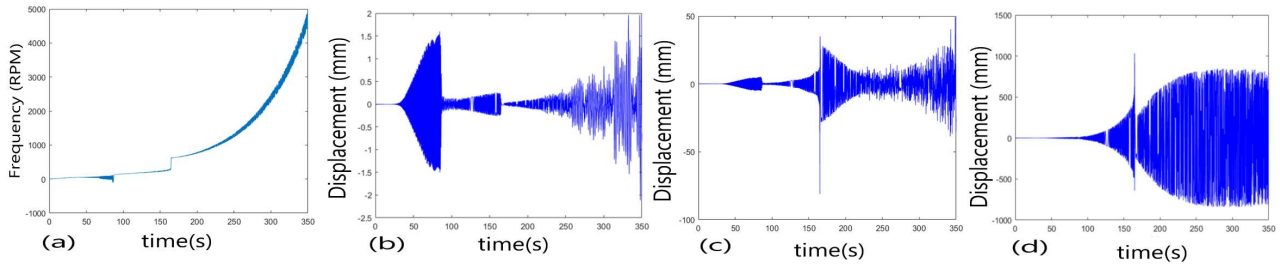

Figure 4.1 Numerical Analysis (a) Angular Velocity, (b) Variable *x*, (c) Variable *y* and (d) Variable *z*

5. EXPERIMENTAL RESULTS

The experimental analysis is carried out in order to verify the existence of behavior similar to that observed by numerical analysis using an apparatus developed and printed on a 3D printer, following the same properties of the mathematical model used.

A 5000 *RPM* 5V *DC* motor is used and speed control is performed with Arduino, where the *DC* motor has an unbalanced mass on its axis, responsible for generating vibrations in the system with an increase in angular velocity, as simulated numerically, the increase in angular velocity is developed by increasing 0.014 V every 1 s, in order to verify the capture of the *DC* motor in the regions of resonance of the structure and reproduce the same time interval used in the analysis numeric.

The angular velocity of the *DC* motor is measured by means of an LM393 (control module photosensitive optical light sensor) and Arduino is responsible for data acquisition, as reported in the materials and methods. For the acquisition of vibration data, it is iPhone 6 cell phone accelerometer was used.

Figure 5.1 represents the configuration used to perform the experimental analysis (a) and the coordinates that are equivalent to the displacement of the cell phone's internal accelerometer used for the acquisition of vibration data in the experiment in (b).

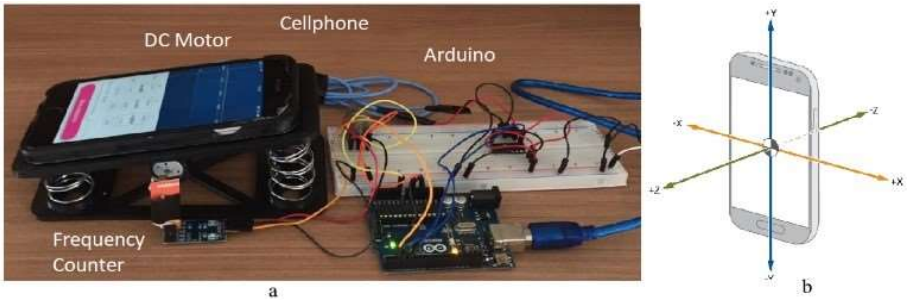

Figure 5.1 Equipment used for the Experimental Analysis (a) and Coordinates of the Mobile (b) (Developed by the Author)

Figure 5.2 (a) shows the evolution of the motor frequency in relation to time. A fluctuation in angular velocity is observed at approximately 75 *s*, with an increase sudden, characteristic of the Sommerfeld effect in approximately 160 *s*, represented in the same figure by a vertical line.

Figure 5.2 (b) that presents the response in time for the variable *x*, demonstrating that the beginning of the *DC* motor capture occurs in approximately 50 *s*. the decrease sudden, characteristic of the Sommerfeld effect is also evidenced in

the figure. Subsequently, a sudden increase in vibrations is observed at approximately 160 *s*. The amplitudes present values that gradually reduce over time, presenting after 220 *s* oscillatory high and low amplitude values.

Figure 5.2 (c) represents the variable *y*, which is equivalent to the transverse displacement of the structure, at the same moments in which the variable *x* is perceived, where the vibration amplitudes increase in approximately 120 *s*, evolving to constant increments until approximately 150 *s*. After this moment, oscillatory values between high and low amplitudes are shown in the figure.

Figure 5.2 (d) represents the displacement on the *z* axis which is equivalent to the linear displacement vertical of the structure. A behavior similar to that observed in the figure is visualized. 5.2 (c), with increasing vibration amplitudes by approximately 50 *s*. the reduction sudden occurs in approximately 60 *s*.

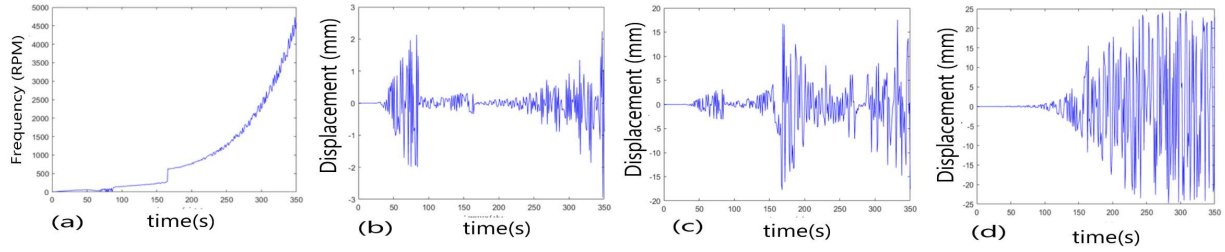

Figure 5.2 Experimental Analysis (a) Angular Velocity, (b) Variable *x*, (c) Variable *y* and (d) Variable *z*

6. CONCLUSION

It is concluded with the development of this work that the physical model used for the experimental analyzes it adheres to the mathematical model used to numerical analyses, although the presented results have different vibration amplitude values. This fact is due to the parametric sensitivity of the system and that some of the parameters of the structure, namely, J_B, J_L, which were adopted in a way empirical and non-linearities that may not have been considered, for example, the coupling of the springs in the structure, and also, the springs themselves.

Figure 6.1 demonstrates the comparison between numerical and experimental analysis for DC motor (a), linear displacement (a) and transverse angular displacement (b) where the numerical results are showed in red and experimental results are showed in blue. It is observed that the increase in the amplitudes of vibrations, characteristic of the Sommerfeld effect, occurs in a similar way for both figures.

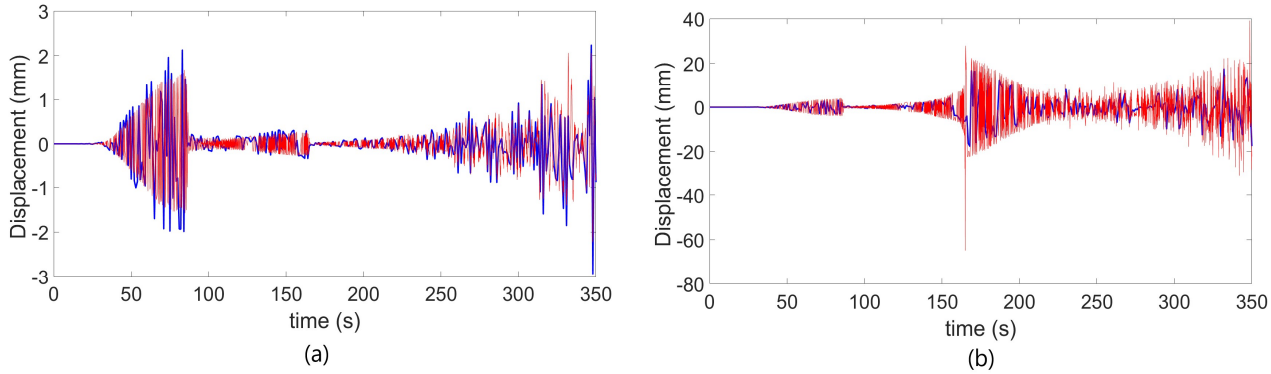

Figure 6.1 Numerical Analysis and Experimental Analysis Comparison

Therefore, it is concluded for future work, more nonlinearities can be added to the structure in order to observe if there will be more similarity in the values of vibration amplitudes. It is also possible to proceed with the development of this research addressing the development of a controller that aims to reduce the influence of the Sommerfeld effect on the structure and in the *DC* motor, and the analysis of the Sommerfeld effect through the graphic demonstration of the vibration amplitudes as a function of the frequency and also, moving the *DC* motor to the end of the mat. Therefore, it is concluded that the objectives proposed initially, which was the verification of the existence of the Sommerfeld effect in the respective conveyor belt, as well as the analysis of the influence of the side effects caused in the *DC* motor and in the structure were achieved satisfactorily.

7. REFERENCES

ALIŞVERIŞÇI, G. F. et al. On dynamic behavior of a nonideal torsional machine suspension structure. In: SPRINGER. Dynamical Systems Theory and Applications. [S.l.], 2015. p. 1–10.

AWREJCEWICZ, J. et al. Dsta-2021 conference books–abstracts. Lodz University of Technology Press, 2021.

BALTHAZAR, J. M. Nonlinear Vibrations Excited by Limited Power Sources. [S.l.]: Springer, 2022

BALTHAZAR, J. M. et al. Remarks on the passage through resonance of a vibrating system with two degrees of freedom, excited by a non-ideal energy source. Journal of Sound and Vibration, v. 239, n. 5, p. 1075–1085, 2001.

BALTHAZAR, J. M. et al. An overview on non-ideal vibrations. Meccanica, Kluwer Academic Publishers, v. 38, n. 6, p. 613–621, 2003.

BALTHAZAR, J. M. et al. An overview on non-ideal vibrations. Meccanica, Kluwer Academic Publishers, v. 38, n. 6, p. 613–621, 2003.

BALTHAZAR, J. M. et al. An overview on the appearance of the sommerfeld effect and saturation phenomenon in non-ideal vibrating systems (nis) in macro and mems scales. Nonlinear Dynamics, Springer, v. 93, n. 1, p. 19–40, 2018.

BISOI, A.; SAMANTARAY, A.; BHATTACHARYYA, R. Control strategies for dc motors driving rotor dynamic systems through resonance. Journal of Sound and Vibration, Elsevier, v. 411, p. 304–327, 2017.

CVETIĆANIN, L. Dynamics of the non-ideal mechanical systems: A review. Journal of the Serbian Society for Computational Mechanics, v. 4, n. 2, p. 75–86, 2010.

FELIX, J. L. P.; BALTHAZAR, J. M. Comments on a nonlinear and nonideal electromechanical damping vibration absorber, sommerfeld effect and energy transfer. Nonlinear Dynamics, Springer, v. 55, n. 1, p. 1–11, 2009.

GONÇALVES, P. et al. The dynamic behavior of a cantilever beam coupled to a non-ideal unbalanced motor through numerical and experimental analysis. Journal of Sound and Vibration, Elsevier, v. 333, n. 20, p. 5115–5129, 2014.

GONÇALVES, P. et al. The dynamic behavior of a cantilever beam coupled to a non-ideal unbalanced motor through numerical and experimental analysis. Journal of Sound and Vibration, Elsevier, v. 333, n. 20, p. 5115–5129, 2014.

GONÇALVES, P. et al. Double resonance capture of a two-degree-of-freedom oscillator coupled to a non-ideal motor. Meccanica, Springer, v. 51, n. 9, p. 2203–2214, 2016.

HUGOT, E. Handbook of cane sugar engineering. [S.l.]: Elsevier, 2014.

KONONENKO, V. O. Vibrating systems with a limited power supply. [S.l.]: Iliffe, 1969.

NAYFEH, A. H.; MOOK, D. T. Nonlinear oscillations. [S.l.]: John Wiley & Sons, 2008.

PETROCINO, E. et al. Vibration control of a cantilever beam coupled to a non-ideal power source by coil impedance matching. In: Advances in Nonlinear Dynamics. [S.l.]: Springer, 2022. p. 221–231.

TSUCHIDA, M. et al. On regular and irregular vibrations of a non-ideal system with two degrees of freedom. 1: 1 resonance. Journal of Sound and Vibration, Elsevier BV, p. 949–960, 2003.

TSUCHIDA, M.; GUILHERME, K. de L.; BALTHAZAR, J. M. On chaotic vibrations of a non-ideal system with two degrees of freedom: 1: 2 resonance and sommerfeld effect. Journal of Sound and Vibration, v. 282, n. 3-5, p. 1201–1207, 2005.

8. RESPONSIBILITY NOTICE

The authors are the only responsible for the printed material included in this paper.